APPLIED SCIENCES AND ENGINEERING

Tuning the deformation mechanisms of boron carbide via silicon doping

Sisi Xiang[1], Luoning Ma[2], Bruce Yang[3], Yvonne Dieudonne[1], George M. Pharr[1], Jing Lu[4], Digvijay Yadav[1], Chawon Hwang[3], Jerry C. LaSalvia[5], Richard A. Haber[3], Kevin J. Hemker[2], Kelvin Y. Xie[1]*

Boron carbide suffers from a loss of strength and toughness when subjected to high shear stresses due to amorphization. Here, we report that a small amount of Si doping (~1 atomic %) leads to a substantial decrease in stress-induced amorphization due to a noticeable change of the deformation mechanisms in boron carbide. In the undoped boron carbide, the Berkovich indentation–induced quasi-plasticity is dominated by amorphization and microcracking along the amorphous shear bands. This mechanism resulted in long, distinct, and single-variant shear faults. In contrast, substantial fragmentation with limited amorphization was activated in the Si-doped boron carbide, manifested by the short, diffuse, and multivariant shear faults. Microcracking via fragmentation competed with and subsequently mitigated amorphization. This work highlights the important roles that solute atoms play on the structural stability of boron carbide and opens up new avenues to tune deformation mechanisms of ceramics via doping.

INTRODUCTION

Boron carbide is widely used in body armor and other engineering applications because of its light weight and high hardness (*1*–*4*). However, consolidated boron carbide loses its strength and toughness when subjected to high-velocity threats (*4*, *5*). The deterioration of the mechanical properties is attributed to the formation of amorphous shear bands, nucleated by high shear stresses generated under impact and sharp-contact loading conditions. These amorphous shear bands act as nucleation sites for microcracks and "the path of the least resistance" for crack propagation, leading to comminuted fracture at much lower stress levels than expected (*4*). Therefore, the ability to control and mitigate amorphization could guide the design of boron carbide–based armor materials with improved ballistic performance.

The susceptibility of amorphization in boron carbide with B_4C stoichiometry could be explained by its atomic configuration. B_4C can be described using a rhombohedral unit cell, consisting of the 12-atom icosahedra connected via the 3-atom chains. The dominant polymorph is thought to be $B_{11}C_p$(CBC), where the C atom in the icosahedra occupies the polar sites (*6*–*11*). Density functional theory (DFT) simulations suggest that the onset of shear-driven amorphization is triggered by the strong interactions of the polar site C atoms in the icosahedra and the B atoms in the chains, which facilitates the unzipping of icosahedra and the destruction of the crystallinity (*6*, *12*). Molecular dynamics simulations predicted that the amorphous B_4C has a higher density than the crystalline phase. When the volume is conserved because of constraints, nanoscale voids/cavities will form and coalesce in the amorphous shear bands, leading to crack opening (*13*). Therefore, tailoring the chain chemistry to reduce the icosahedron-chain interactions offers a promising pathway for mitigating amorphization and subsequently suppressing the anomalous failure in boron carbide.

One effective strategy to modify the chain chemistry and structure is microalloying, such as Si doping (*14*–*19*). Recently, Khan *et al.* (*16*) successfully synthesized bulk single-phase Si-doped boron carbide. Rietveld refinement analysis of the x-ray diffraction results revealed that Si atoms occupied the chain sites, forming kinked CSiC chains. DFT simulations predicted that Si doping stabilizes icosahedra from collapsing upon shearing and should lead to improved amorphization resistance (*15*, *16*). However, experimental evidence that verifies this prediction has not been conducted, although some encouraging preliminary observations have been made (*17*). Moreover, the underpinning mechanisms of how Si doping mitigates amorphization at the microstructure level are unknown.

In the present work, we experimentally characterized the effects of Si doping on the deformation behavior of boron carbide. We created a diffusion couple using boron carbide (with millimeter grain sizes) and silicon hexaboride (SiB_6) to achieve a Si concentration gradient within one boron carbide grain. We then used nanoindentation to induce amorphization and applied advanced microscopy techniques to uncover the microstructure of the quasi-plastic zones from both the undoped and Si-doped regions. We observed that a small amount of Si doping [~1 atomic % (at %)] led to a substantial decrease in stress-induced amorphization. More unexpectedly, Si doping also markedly changed the deformation mechanisms in boron carbide.

RESULTS AND DISCUSSION

Energy-dispersive x-ray spectroscopy (EDS) revealed that the Si-diffused zone is approximately 250 μm in the boron carbide–SiB_6 diffusion couple (Fig. 1A and fig. S2). The millimeter boron carbide grains and the ~250-μm diffusion zone allow a Si concentration gradient in single grains. All the nanoindentation tests, microstructural analyses, and comparisons were carried out in the same boron carbide grain. This experimental design ensures that the observed differences can be dominantly attributed to Si doping. The roles of other variables such as crystal orientation and grain boundaries are precluded.

[1]Department of Materials Science and Engineering, Texas A&M University, College Station, TX 77843, USA. [2]Department of Mechanical Engineering, Johns Hopkins University, Baltimore, MD 21218, USA. [3]Department of Materials Science and Engineering, Rutgers University, Piscataway, NJ 08854, USA. [4]NanoMEGAS USA, Tempe, AZ 85281, USA. [5]U.S. Army Research Laboratory, Aberdeen Proving Ground, Aberdeen, MD 21005, USA.
*Corresponding author. Email: kelvin_xie@tamu.edu

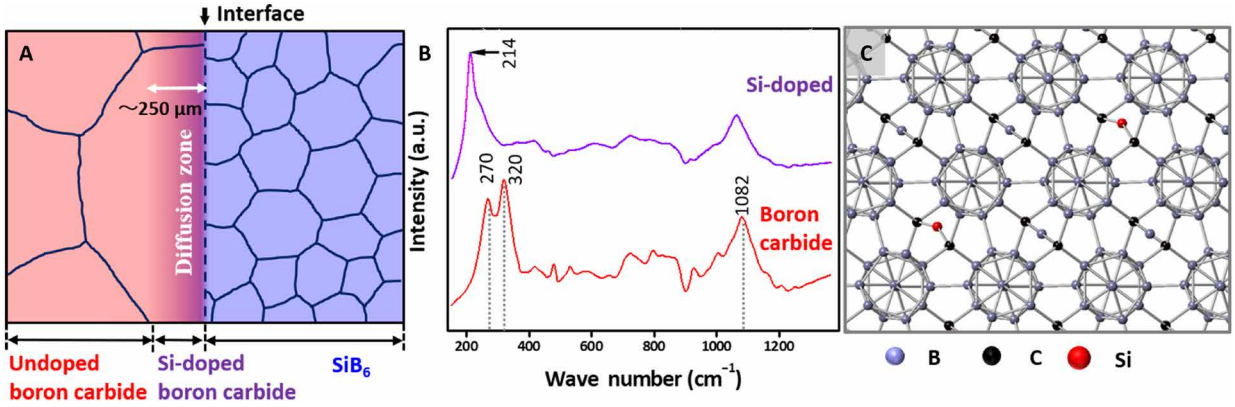

Fig. 1. Structure characteristics of the arc-melted sample after diffusion. (**A**) Schematic of the arc-melted sample after diffusion has taken place. (**B**) Raman spectra for undoped boron carbide and Si-doped boron carbide. a.u., arbitrary units. (**C**) A possible atomic model of the Si-doped boron carbide. Some of the CBC chains are replaced by kinked CSiC chains. [The model is adopted from (*16*).]

Representative Raman spectra obtained from the undoped boron carbide and Si-doped boron carbide highlighted the differences in their chemical bonding (Fig. 1B). A typical Raman spectrum of the undoped boron carbide displays major peaks at 270, 320, and 1082 cm^{-1}. The Raman spectra acquired from the Si diffusion zone also showed a notable peak at 1082 cm^{-1}. However, the intensities of the 270- and 320-cm^{-1} peaks were much lower. A new peak at 214 cm^{-1} was also observed. It is suggested that, for boron carbide, the high-frequency peaks (e.g., 1082 cm^{-1}) are attributed to the "breathing" mode of icosahedra, while the low-frequency peaks (e.g., 200 to 350 cm^{-1}) correspond to the chains (*9*–*11*, *20*). The fact that the high-frequency peak remained the same but the low-frequency peaks changed markedly indicates that the icosahedra were retained while the chains were modified via Si doping. The observed Raman spectra for both undoped boron carbide and Si-doped boron carbide are similar to what have been reported in the literature (*16*, *20*). An atomic model describing the B, C, and Si atomic occupancy in the Si-doped boron carbide is provided in Fig. 1C, where some of the CBC chains are replaced by kinked CSiC chains, as described by Khan *et al.* (*16*).

Having both the undoped and Si-doped regions in the same boron carbide grain, we then used Vickers indentation and Raman mapping to assess whether Si doping could mitigate amorphization. Indentation with sharp indenter tips (such as Vickers and Berkovich) is a common technique to impose large shear stress and to trigger stress-induced amorphization in boron carbide (*15*, *21*–*25*). Raman spectroscopy was then performed on the residual imprints. New peaks (such as 1320, 1520, and 1800 cm^{-1}) associated with amorphization were noted in all indents but were less prominent for the indents in the Si-doped region (Fig. 2, A and B). Figure 2 (C and D) depicts the amorphization intensity maps, where each pixel is plotted on the basis of the normalized intensity of the bands at ~1800 cm^{-1} from the indents and the regions in the vicinity of the indents (*21*, *26*). Bands (1320 and 1520 cm^{-1}) were excluded from this analysis because of their shared peak positions with the graphitic carbon peaks. It is evident that the degree and extent of amorphization was markedly reduced in the Si-doped area compared to the undoped boron carbide. This observation is in good agreement with the DFT predictions (*14*, *16*) and previous nonhydrostatic diamond-anvil experimental results, where nonhydrostatic stresses were applied on the undoped and Si-doped boron carbide (*17*).

To understand why Si doping facilitates amorphization mitigation at the microstructure level, cross-sectional transmission electron microscopy (TEM) foils were prepared from the Berkovich nanoindentations using the focused ion beam (FIB) lift-out method. This approach was not attempted on the Vickers indents because previous experience has shown that large residual stresses and numerous cracks prohibit a successful lift-out. Nonetheless, nanoindentation tests with Berkovich tips could also effectively induce amorphization in boron carbide (*23*–*25*, *27*). Moreover, nanoindentation offers insight on the mechanical properties (*28*). The hardness of Si-doped boron carbide at 500 mN (~50 GPa) is comparable to that of the undoped counterpart (for details, see fig. S3A). Compared with the undoped boron carbide, the Si-doped boron carbide has become slightly softer, which was shown in typical nanoindentation load-displacement curves for undoped and Si-doped boron carbides (fig. S3B). TEM foils were prepared from the indents at ~300 μm (undoped) and ~120 μm (Si-doped) away from the diffusion interface. The Si content present in the Si-doped specimens was measured using EDS and semi-quantitatively estimated to be 1 at %.

Quasi-plastic zones induced by Berkovich nanoindentation were observed in both the undoped and Si-doped boron carbide (for example from the same grain, see Fig. 3; for the corresponding bright-field scanning TEM images, see fig. S4). A quick inspection of their microstructure may leave the impression that they are similar. All quasi-plastic zones exhibit complicated diffraction contrast due to the large plastic deformation and elastic residual strain. However, imaging with higher magnification revealed that the characteristics of the amorphous shear bands and microcracks in the quasi-plastic zones are notably different. Careful inspection of the indented undoped boron carbide showed many long, distinct, and dominantly single-variant shear faults (i.e., amorphous shear bands and microcracks), as shown in Fig. 3C. This finding is consistent with the literature (*15*, *25*). In contrast, short and multivariant shear faults contributed to the quasi-plasticity in the Si-doped sample (Fig. 3D). The prominent differences suggest that as low as 1 at % Si doping may markedly change the deformation mechanisms in boron carbide. However, we encounter a predicament here. Lower-magnification TEM images offer an overall view, whereas higher magnification only reveals a very localized microstructure. While the former makes it difficult to discern the complicated contrast, the latter makes it difficult to confirm whether the observed features are representative. To overcome this challenge, we used an advanced TEM-based diffraction technique, precession electron diffraction (PED), to

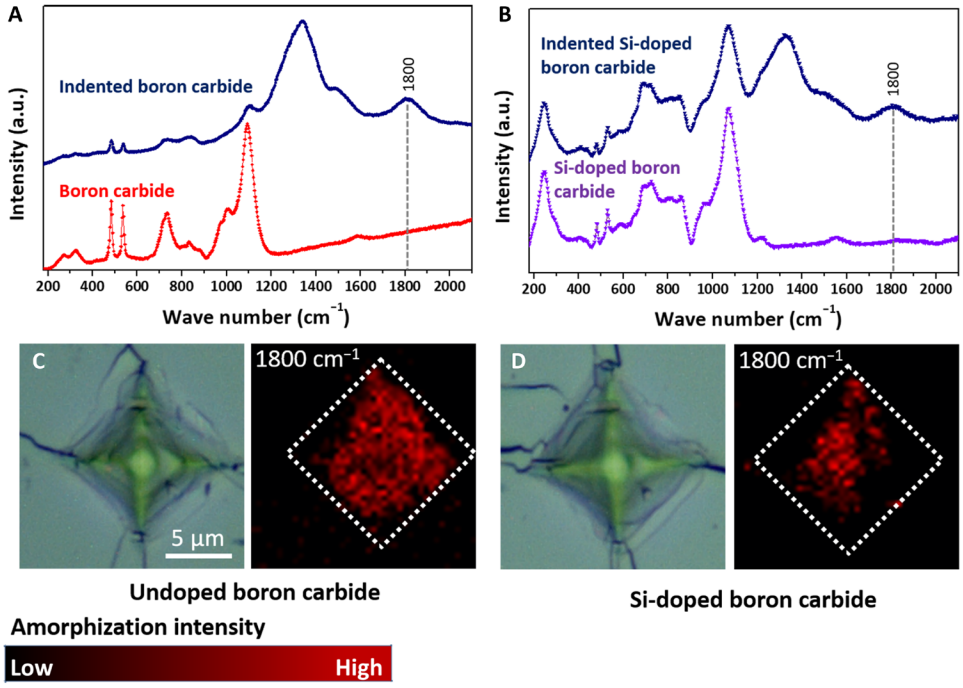

Fig. 2. Comparison of the Raman spectra of indented undoped and Si-doped boron carbides underneath the Vickers indents. Raman spectra of indented (**A**) undoped boron carbide and (**B**) Si-doped boron carbide compared to their pristine counterparts. Raman mapping of the amorphous phase in Vickers hardness impressions in (**C**) undoped boron carbide and within the diffusion zone and (**D**) in Si-doped single-crystal boron carbide.

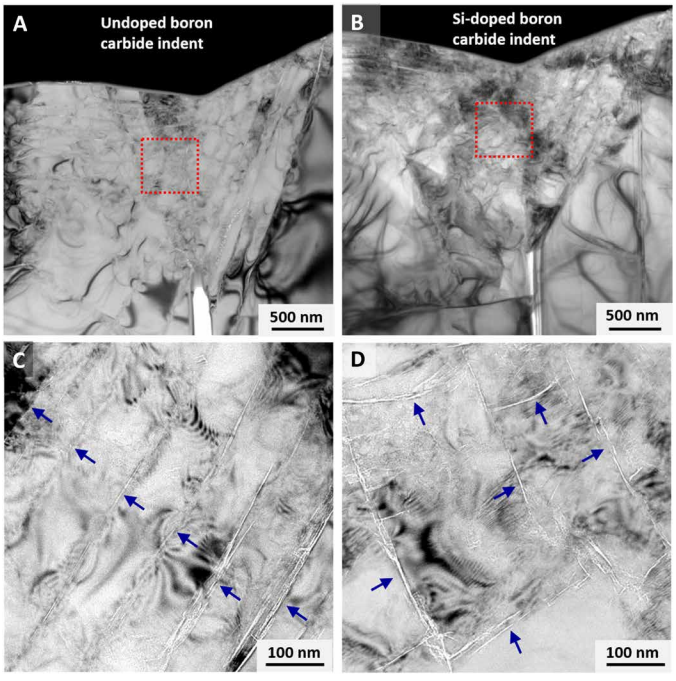

Fig. 3. Bright-field TEM images of indented undoped and Si-doped boron carbides. Low-magnification TEM images of indented (**A**) undoped and (**B**) Si-doped boron carbides, with higher-magnification images showing shear faults in (**C**) and (**D**), respectively. The shear faults (consisting of amorphous bands and microcracks) are indicated by the arrows.

simultaneously obtain the global and local microstructure of the quasi-plastic zones.

The orientation, reliability, and correlation coefficient information derived from the PED results highlighted the microstructural similarities and differences of the quasi-plastic zones in the undoped and Si-doped boron carbide. Crystal reorientation was observed in all quasi-plastic zones compared to the corresponding pristine zones (Fig. 4, A and B), which can be attributed to the amorphous shear bands and microcracks (*4*, *23*, *29*). Orientation maps viewed in all three principal directions can be found in fig. S5. Closer inspections unveiled the differences. In the reliability maps (superimposed with the orientation maps; for details, see Materials and Methods), we note that most pixels in the quasi-plastic zones of the undoped boron carbide display high reliability. The low-reliability pixels are generally associated with the long and distinct amorphous bands and microcracks (Fig. 4A). They are better illuminated in the correlation coefficient maps (Fig. 4B), confirming that these long, distinct, and single-variant shear faults (along each side of the indent impression) are the prevailing microstructural features in the quasi-plastic zones in undoped boron carbide. On the contrary, for the Si-doped boron carbide, most amorphous shear bands and microcracks are much more diffuse and difficult to distinguish (Fig. 4, C and D). Although some shear faults are still present in the quasi-plastic zones (such as the top left region near the impression surface in Fig. 4, C and D), they are no longer the predominant features. Combined with the higher-magnification bright-field TEM observations, we can deduce that short, diffuse, and multivariant shear faults are prevalent in the quasi-plastic zones of Si-doped boron carbide samples. In addition, a number of low-reliability regions are evident (Fig. 4C). More detailed analysis showed that they are caused by multiple sets of diffraction patterns through

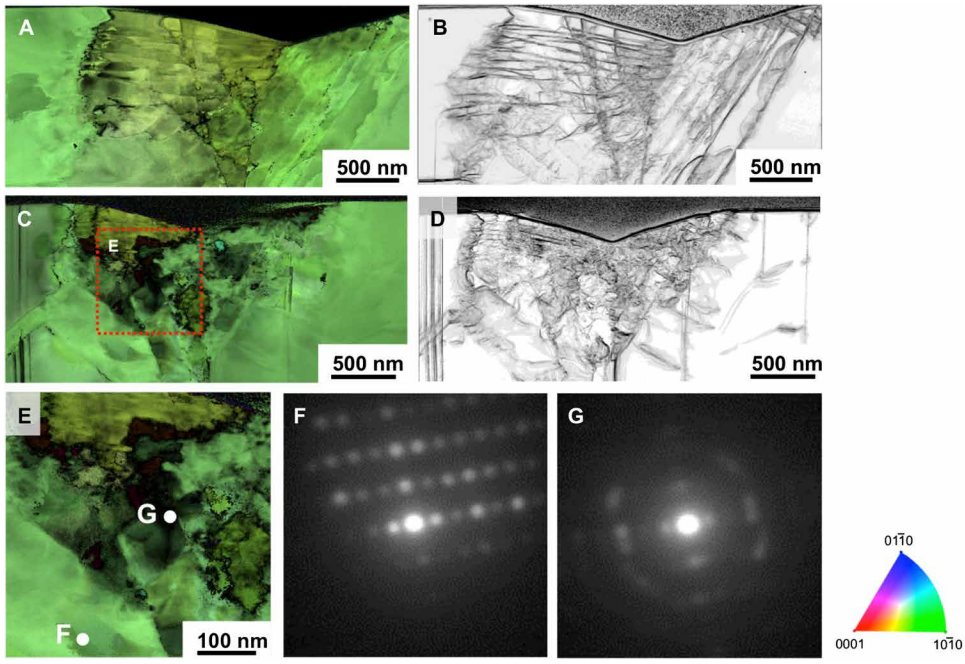

Fig. 4. Microstructure of the quasi-plastic zones revealed by PED with a step size of 5 nm. (**A**) Orientation map overlapped with reliability map and (**B**) correlation coefficient map of undoped boron carbide. (**C**) Orientation map overlapped with reliability map and (**D**) correlation coefficient map of Si-doped boron carbide. (**E**) Orientation and reliability map containing part of the quasi-plastic zone of a Si-doped boron carbide sample. The corresponding diffraction patterns from the regions (**F**) outside and (**G**) inside the quasi-plastic zone, as labeled in (E). The orientation maps are viewed along the out-of-plane direction. (Note that the intensity of diffuse ring from the narrow amorphous shear bands is overpowered by the diffraction spots from the crystalline phase. The amorphous nature of the shear bands is best revealed by high-resolution TEM rather than PED.)

the thickness of the TEM foil (Fig. 4, E to G). This observation infers that many shear faults have large proportions of fault planes contained within the TEM foil. Overlapping crystals were not observed in undoped boron carbide. This further confirms the multivariant nature of the shear faults in the Si-doped samples. As been described previously, the indents that we examined were from the same boron carbide grain but with varied chemistry. Therefore, the differences in deformation behavior are primarily caused by Si doping.

To explain the remarkable differences in microstructure and to deduce the active deformation mechanisms, we quantified the densities of shear faults (dividing the total shear fault length by the area) from the same regions in the undoped and Si-doped quasi-plastic zones. The average length density of shear faults was measured to be $9.3 \pm 3.5\,\mu m^{-1}$ in the undoped boron carbide and $10.8 \pm 2.4\,\mu m^{-1}$ in the Si-doped boron carbide. Two-sample t test suggested that the shear fault densities are statistically the same in both samples. (The calculated $|T|$ is equal to 1.23, which is less than the critical value of $t_{1-\alpha/2,\nu} = 2.365$ for the two-tailed t distribution.) The Raman results indicated that Si doping provides substantial amorphization mitigation, but the TEM observation revealed that Si doping did not reduce the shear fault density. The seeming ambivalence suggests that many microcracks in the Si-doped samples are caused by direct fragmentation rather than amorphization. The change in mechanism is also manifested by morphologies of shear faults. The shear faults in the undoped boron carbide quasi-plastic zones are long, straight, distinct, and dominantly single variant, indicating that they started as amorphous shear bands and evolved in microcracks. The high planarity of the shear faults is dictated by the fact that amorphous shear bands generally grow along specific crystallographic planes (*4*, *23*). In contrast, the shear faults in the Si-doped boron carbide are short, meandering, diffuse, and multivariant, suggesting that many of them were not evolved from amorphous shear bands but directly formed from fragmentation. The hardness values of the undoped and Si-doped boron carbide regions are comparable. This implies that at similar stress levels, amorphization was dominant in the undoped boron carbide, whereas both amorphization and fragmentation were activated in the Si-doped boron carbide. The presence of Si in the lattice may have stabilized the icosahedra against amorphization (*15*, *16*) and lowered the energy barrier for fragmentation via atomic-level local lattice distortion (*16*). Because amorphization could lead to a sudden deterioration of mechanical properties (*4*), while regular fragmentation does not (*5*, *30*), Si doping may present itself a promising strategy to design boron carbide exhibiting superior ballistic performance.

In summary, we discovered that even a small amount of Si doping (~1 at %) in boron carbide resulted in a marked change in the deformation mechanisms. Si doping led to a reduction of stress-induced amorphization in boron carbide. We also observed that long, distinct, and dominantly single-variant shear faults formed in the quasi-plastic zones of the undoped boron carbide; short, diffuse, and multivariant shear faults contributed to the quasi-plasticity in the Si-doped sample. The mitigation of amorphization and the change in deformation mechanisms are likely caused by the atomic-level structural stabilization and lowering energy barrier for fragmentation from Si doping. These discoveries could guide the design of next-generation amorphization-resistant body armor. Moreover, the insight gained from this work opens up pathways for tuning the deformation mechanisms of ceramics via solute doping.

MATERIALS AND METHODS

Bulk boron carbide was prepared using a commercial (5SA) benchtop 300 Amp arc melter. Commercial (Starck, Grade HD20) boron carbide powder (0.5 g) was first cold-pressed into a pellet and then melted in an argon flow. As the liquid cooled, millimeter-sized boron carbide crystals were formed on the surface of the ingot (fig. S1A). A 5 mm × 5 mm × 5 mm cube was sectioned from the ingot and polished to mirror finish using diamond suspensions. The boron carbide cube was coupled with a cold-pressed SiB_6 (Starck, grade A) pellet and heat-treated in a spark plasma sintering apparatus at 1700°C for 4 hours under 50 MPa (for the schematic, see fig. S1B). After heating, the diffusion couple was sectioned parallel to the diffusion direction and polished to mirror finish for further microscopy analyses.

Raman spectroscopy equipped with a 633-nm HeNe laser (InVia Reflex, Renishaw, UK) was used to identify the phases present within the diffusion zone and the material on either side of the zone as well as the amorphized materials in the indents (Figs. 1 and 2). WIRE 4.2 software was used to deconvolute the Raman spectra and assess the extent of amorphization. Electron backscatter diffraction (EBSD) was performed to measure the boron carbide grain size after diffusion had taken place. EDS was used to semiquantitatively measure the Si content in the diffusion zone. The exact Si content is difficult to obtain using EDS because of the presence of light elements such as B and C in the specimen. Before nanoindentation, the diffusion couple sample polished to mirror finish using diamond lapping film (from 30 to 1 μm). Nanoindentation was performed at room temperature using both Vickers and Berkovich indenters. Vickers indents (1 kg) and 500-mN Berkovich indents (constant loading rate of 25 mN/s) were placed across the Si-doped diffusion zone and the undoped boron carbide. When measuring the degree of amorphization, Raman spectroscopy was only performed on the Vickers indents as the Berkovich indents are too small. Some of the Berkovich indents were used for TEM observations.

The cross-sectional TEM samples of undoped and Si-doped boron carbide were prepared from the residual indents using a Tescan LYRA-3 Model GMH dual-beam FIB instrument. TEM observation was conducted in a FEI Tecnai G2 F20 Super-Twin FE-TEM operating at 200 kV. Elemental analyses of the TEM samples were carried out using EDS in the TEM. The Si contents were measured in both Si-free and Si-doped specimens to ensure that the Si signal was from doping and not from the Si present in the EDS detector. Again, EDS is not the ideal chemical analysis technique in this study. Nevertheless, it served as a semiquantitative method to estimate the Si content in the Si-doped boron carbide.

The PED experiments were performed using a FEI Tecnai TF30 transmission electron microscope equipped with a NanoMEGAS ASTAR system (*31*, *32*). Three types of maps (orientation, reliability, and correlation coefficient) were constructed from the PED results with the 5-nm scanning step size in all samples. The orientation maps are similar to the inverse pole figures in EBSD scans, in which the color of each pixel represents its orientation. In reliability maps, the experimentally acquired diffraction pattern was compared to the simulated pattern in the database. Low brightness indicates a poor match. Poor matches can be caused by the lack of diffraction spots (e.g., amorphous phase and microcracks) and multiple sets of diffraction spots (e.g., crystals overlapping). In the correlation coefficient maps, the diffraction pattern of each pixel is compared to the patterns of its nearest neighbors, and changes in microstructure, such as amorphous phase, microcracks, grain boundaries, and elastic strain, are highlighted.

SUPPLEMENTARY MATERIALS

Supplementary material for this article is available at http://advances.sciencemag.org/cgi/content/full/5/10/eaay0352/DC1

Fig. S1. Preparation of the diffusion couple.
Fig. S2. Berkovich nanoindentation was performed across the Si diffusion zone and the undoped boron carbide within one boron carbide grain.
Fig. S3. Berkovich nanoindentation results for undoped and Si-doped boron carbides.
Fig. S4. TEM observation of indented undoped and Si-doped boron carbides.
Fig. S5. Orientation maps of the quasi-plastic zones of undoped and Si-doped boron carbides.

REFERENCES AND NOTES

1. V. Domnich, S. Reynaud, R. A. Haber, M. Chhowalla, Boron carbide: Structure, properties, and stability under stress. *J. Am. Ceram. Soc.* **94**, 3605–3628 (2011).
2. K. Y. Xie, K. Kuwelkar, R. A. Haber, J. C. LaSalvia, K. J. Hemker, Microstructural characterization of a commercial hot-pressed boron carbide armor plate. *J. Am. Ceram. Soc.* **99**, 2834–2841 (2016).
3. M. W. Chen, J. W. McCauley, J. C. LaSalvia, K. J. Hemker, Microstructural characterization of commercial hot-pressed boron carbide ceramics. *J. Am. Ceram. Soc.* **88**, 1935–1942 (2005).
4. M. Chen, J. W. McCauley, K. J. Hemker, Shock-induced localized amorphization in boron carbide. *Science* **299**, 1563–1566 (2003).
5. D. E. Grady, Shock-wave strength properties of boron carbide and silicon carbide. *J. Phys. IV* **4**, C8-385–C8-391 (1994).
6. Q. An, W. A. Goddard III, T. Cheng, Atomistic explanation of shear-induced amorphous band formation in boron carbide. *Phys. Rev. Lett.* **113**, 095501 (2014).
7. G. Fanchini, J. W. McCauley, M. Chhowalla, Behavior of disordered boron carbide under stress. *Phys. Rev. Lett.* **97**, 035502 (2006).
8. C. Kunka, A. Awasthi, G. Subhash, Crystallographic and spectral equivalence of boron-carbide polymorphs. *Scr. Mater.* **122**, 82–85 (2016).
9. H. Werheit, Boron carbide: Consistency of components, lattice parameters, fine structure and chemical composition makes the complex structure reasonable. *Solid State Sci.* **60**, 45–54 (2016).
10. H. Werheit, A. Leithe-Jasper, T. Tanaka, H. W. Rotter, K. A. Schwetz, Some properties of single-crystal boron carbide. *J. Solid State Chem.* **177**, 575–579 (2004).
11. H. Werheit, S. Shalamberidze, Advanced microstructure of boron carbide. *J. Phys. Condens. Matter* **24**, 385406 (2012).
12. K. Y. Xie, Q. An, T. Sato, A. J. Breen, S. P. Ringer, W. A. Goddard III, J. M. Cairney, K. J. Hemker, Breaking the icosahedra in boron carbide. *Proc. Natl. Acad. Sci. U.S.A.* **113**, 12012–12016 (2016).
13. Q. An, W. A. Goddard III, Atomistic origin of brittle failure of boron carbide from large-scale reactive dynamics simulations: Suggestions toward improved ductility. *Phys. Rev. Lett.* **115**, 105501 (2015).
14. Q. An, W. A. Goddard III, Microalloying boron carbide with silicon to achieve dramatically improved ductility. *J. Phys. Chem. Lett.* **5**, 4169–4174 (2014).
15. G. Subhash, A. P. Awasthi, C. Kunka, P. Jannotti, M. DeVries, In search of amorphization-resistant boron carbide. *Scr. Mater.* **123**, 158–162 (2016).
16. A. U. Khan, A. M. Etzold, X. Yang, V. Domnich, K. Y. Xie, C. Hwang, K. D. Behler, M. Chen, Q. An, J. C. LaSalvia, K. J. Hemker, W. A. Goddard III, R. A. Haber, Locating Si atoms in Si-doped boron carbide: A route to understand amorphization mitigation mechanism. *Acta Mater.* **157**, 106–113 (2018).
17. J. E. Proctor, V. Bhakhri, R. Hao, T. J. Prior, T. Scheler, E. Gregoryanz, M. Chhowalla, F. Giulani, Stabilization of boron carbide via silicon doping. *J. Phys. Condens. Matter* **27**, 015401 (2014).
18. M. K. Kolel-Veetil, R. M. Gamache, N. Bernstein, R. Goswami, S. B. Qadri, K. P. Fears, J. B. Miller, E. R. Glaser, T. M. Keller, Substitution of silicon within the rhombohedral boron carbide (B_4C) crystal lattice through high-energy ball-milling. *J. Mater. Chem. C* **3**, 11705–11716 (2015).
19. C. J. Marvel, K. D. Behler, J. C. LaSalvia, V. Domnich, R. A. Haber, M. Watanabe, M. P. Harmer, Extending ζ-factor microanalysis to boron-rich ceramics: Quantification of bulk stoichiometry and grain boundary composition. *Ultramicroscopy* **202**, 163–172 (2019).
20. K. Y. Xie, V. Domnich, L. Farbaniec, B. Chen, K. Kuwelkar, L. Ma, J. W. McCauley, R. A. Haber, K. T. Ramesh, M. Chen, K. J. Hemker, Microstructural characterization of boron-rich boron carbide. *Acta Mater.* **136**, 202–214 (2017).
21. G. Parsard, G. Subhash, Raman spectroscopy mapping of amorphized zones beneath static and dynamic Vickers indentations on boron carbide. *J. Eur. Ceram. Soc.* **37**, 1945–1953 (2017).
22. G. Parsard, G. Subhash, P. Jannotti, Amorphization-induced volume change and residual stresses in boron carbide. *J. Am. Ceram. Soc.* **101**, 2606–2615 (2018).
23. K. M. Reddy, P. Liu, A. Hirata, T. Fujita, M. W. Chen, Atomic structure of amorphous shear bands in boron carbide. *Nat. Commun.* **4**, 2483 (2013).

24. V. Domnich, Y. Gogotsi, M. Trenary, T. Tanaka, Nanoindentation and Raman spectroscopy studies of boron carbide single crystals. *Appl. Phys. Lett.* **81**, 3783–3785 (2002).
25. D. Ge, V. Domnich, T. Juliano, E. A. Stach, Y. Gogotsi, Structural damage in boron carbide under contact loading. *Acta Mater.* **52**, 3921–3927 (2004).
26. G. Subhash, D. Ghosh, J. Blaber, J. Q. Zheng, K. Masters, Characterization of the 3-D amorphized zone beneath a Vickers indentation in boron carbide using Raman spectroscopy. *Acta Mater.* **61**, 3888–3896 (2013).
27. V. Domnich, Y. Gogotsi, S. Dub, Effect of phase transformations on the shape of the unloading curve in the nanoindentation of silicon. *Appl. Phys. Lett.* **76**, 2214–2216 (2000).
28. W. C. Oliver, G. M. Pharr, An improved technique for determining hardness and elastic modulus using load and displacement sensing indentation experiments. *J. Mater. Res.* **7**, 1564–1583 (1992).
29. C. Kunka, Q. An, N. Rudawski, G. Subhash, J. Zheng, V. Halls, J. Singh, Nanotwinning and amorphization of boron suboxide. *Acta Mater.* **147**, 195–202 (2018).
30. D. E. Grady, Hugoniot equation of state and dynamic strength of boron carbide. *J. Appl. Phys.* **117**, 165904 (2015).
31. E. F. Rauch, M. Veron, Coupled microstructural observations and local texture measurements with an automated crystallographic orientation mapping tool attached to a tem. *Materialwiss. Werkst.* **36**, 552–556 (2005).
32. E. F. Rauch, J. Portillo, S. Nicolopoulos, D. Bultreys, S. Rouvimov, P. Moeck, Automated nanocrystal orientation and phase mapping in the transmission electron microscope on the basis of precession electron diffraction. *Z. Kristallogr.* **225**, 103–109 (2010).

Acknowledgments

Funding: This study was partly sponsored by the Defense Advanced Research Projects Agency under grant no. W31P4Q-13-1-0001. Additional support was received from K.Y.X.'s start-up grant from Texas A&M Engineering Experiment Station (TEES). **Author contributions:** K.Y.X., R.A.H., and K.J.H. designed research. S.X., L.M., B.Y., Y.D., G.M.P., J.L., D.Y., C.H., J.C.L., R.A.H., K.J.H., and K.Y.X. performed research. S.X., L.M., B.Y., Y.D., G.M.P., J.L., D.Y., C.H., J.C.L., R.A.H., K.J.H., and K.Y.X. analyzed data. S.X., L.M., B.Y., Y.D., G.M.P., J.L., D.Y., C.H., J.C.L., R.A.H., K.J.H., and K.Y.X. wrote the paper. All authors reviewed and approved the manuscript. **Competing interests:** The authors declare that they have no competing interests. **Data and materials availability:** All data needed to evaluate the conclusions in the paper are present in the paper and/or the Supplementary Materials. Additional data related to this paper may be requested from the authors. Experimental data are stored on a password-protected computer and backed up on a network-attached storage drive located at Texas A&M University.

Submitted 15 May 2019
Accepted 16 September 2019
Published 25 October 2019
10.1126/sciadv.aay0352

Citation: S. Xiang, L. Ma, B. Yang, Y. Dieudonne, G. M. Pharr, J. Lu, D. Yadav, C. Hwang, J. C. LaSalvia, R. A. Haber, K. J. Hemker, K. Y. Xie, Tuning the deformation mechanisms of boron carbide via silicon doping. *Sci. Adv.* **5**, eaay0352 (2019).